The Astronomical Journal, 141:73 (12pp), 2011 March doi:10.1088/0004-6256/141/3/73

DENSE CLUMPS IN GIANT MOLECULAR CLOUDS IN THE LARGE MAGELLANIC CLOUD: DENSITY AND TEMPERATURE DERIVED FROM ^{13}CO(J = 3–2) OBSERVATIONS

Tetsuhiro Minamidani[1,2], Takanori Tanaka[3], Yoji Mizuno[3], Norikazu Mizuno[4], Akiko Kawamura[3], Toshikazu Onishi[5], Tetsuo Hasegawa[4], Ken'ichi Tatematsu[4], Tatsuya Takekoshi[2], Kazuo Sorai[1,2], Nayuta Moribe[3], Kazufumi Torii[3], Takeshi Sakai[6], Kazuyuki Muraoka[5], Kunihiko Tanaka[7], Hajime Ezawa[4], Kotaro Kohno[6], Sungeun Kim[8], Mónica Rubio[9], and Yasuo Fukui[3]

[1] Department of Physics, Faculty of Science, Hokkaido University, N10W8, Kita-ku, Sapporo 060-0810, Japan; tetsu@astro1.sci.hokudai.ac.jp
[2] Department of Cosmosciences, Graduate School of Science, Hokkaido University, N10W8, Kita-ku, Sapporo 060-0810, Japan
[3] Department of Astrophysics, Nagoya University, Furo-cho, Chikusa-ku, Nagoya 464-8602, Japan
[4] National Astronomical Observatory of Japan, Mitaka, Tokyo 181-8588, Japan
[5] Department of Physical Science, Osaka Prefecture University, Gakuen 1-1, Sakai, Osaka 599-8531, Japan
[6] Institute of Astronomy, The University of Tokyo, 2-21-1 Osawa, Mitaka, Tokyo 181-0015, Japan
[7] Institute of Science and Technology, Keio University, 4-14-1 Hiyoshi, Yokohama, Kanagawa 223-8522, Japan
[8] Astronomy and Space Science Department, Sejong University, 98 Kwangjin-gu, Kunja-dong, Seoul 143-747, Republic of Korea
[9] Departament de Astronomía, Universidad de Chile, Casilla 36-D, Santiago, Chile
Received 2010 September 28; accepted 2010 December 17; published 2011 January 31

ABSTRACT

In order to precisely determine the temperature and density of molecular gas in the Large Magellanic Cloud, we made observations of the optically thin ^{13}CO(J = 3–2) transition using the ASTE 10 m telescope toward nine peaks where ^{12}CO(J = 3–2) clumps were previously detected with the same telescope. The molecular clumps include those in giant molecular cloud (GMC) Types I (with no signs of massive star formation), II (with H II regions only), and III (with H II regions and young star clusters). We detected ^{13}CO(J = 3–2) emission toward all the peaks and found that their intensities are 3–12 times lower than those of ^{12}CO(J = 3–2). We determined the intensity ratios of ^{12}CO(J = 3–2) to ^{13}CO(J = 3–2), $R_{3-2}^{12/13}$, and ^{13}CO(J = 3–2) to ^{13}CO(J = 1–0), $R_{3-2/1-0}^{13}$, at 45″ resolution. These ratios were used in radiative transfer calculations in order to estimate the temperature and density of the clumps. The clumps have a kinetic temperature range of $T_{\rm kin}$ = 15–200 K and a molecular hydrogen gas density range of $n(\rm H_2) = 8 \times 10^2$–$7 \times 10^3$ cm^{-3}. We confirmed that the higher density clumps have higher kinetic temperature and that the lower density clumps have lower kinetic temperature to better accuracy than in previous work. The kinetic temperature and density increase generally from a Type I GMC to a Type III GMC. We interpret that this difference reflects an evolutionary trend of star formation in molecular clumps. The $R_{3-2/1-0}^{13}$ and kinetic temperature of the clumps are well correlated with the Hα flux, suggesting that the heating of molecular gas with density $n(\rm H_2) = 10^3$–10^4 cm^{-3} can be explained by stellar far-ultravoilet photons.

Key words: galaxies: individual (LMC) – ISM: clouds – ISM: molecules – Magellanic Clouds – radio lines: ISM – submillimeter: general

Online-only material: color figures

1. INTRODUCTION

Star formation is of fundamental importance in understanding the evolution of galaxies. Stars are formed in dense clumps of giant molecular clouds (GMCs), and kinetic energy and heavy elements are ejected from stars back into the interstellar medium (ISM) through stellar winds and supernova explosions. This cycle enriches metal abundance in the ISM and drives the evolution of galaxies both physically and chemically. It is therefore important to better understand the evolution of GMCs, the principal sites of star formation in galaxies.

The Large Magellanic Cloud (LMC) is the most suitable galaxy for the study of star formation and natal GMCs since it offers a unique opportunity to achieve the highest resolution due to its proximity, 50 kpc (Keller & Wood 2006; Feast 1999), and nearly face-on position with an inclination angle of ∼35°(van der Marel & Cioni 2001). This also provides an advantage of less contamination along the line of sight. The LMC shows active on-going star formation and many massive young clusters being formed (Hodge 1961). In the LMC, the metallicity is a factor of ∼3–4 lower (Dufour 1984; Rolleston et al. 2002) and the gas-to-dust ratio is a factor of ∼4 higher (Koornneef 1984) than values for the solar neighborhood. The far-ultraviolet (FUV) radiation field is more intense in the LMC than in the Milky Way (Israel et al. 1986) and the visual extinction is a few times lower. These influence the physical properties of GMCs and may affect the initial conditions for star and cluster formation.

The first spatially resolved surveys of GMCs in the LMC were made by the NANTEN 4 m telescope in the ^{12}CO(J = 1–0) transition (Fukui et al. 1999, 2001, 2008; Mizuno et al. 2001). These surveys revealed the distribution of GMCs within a single galaxy at ∼40 pc resolution. Fukui et al. (2008) derived the physical properties, such as size, line width, and virial mass, of the GMCs and found that the ^{12}CO(J = 1–0) luminosity and virial mass of the clouds show a good correlation. Assuming that the clouds are in virial equilibrium, Fukui et al. (2008) derived the $X_{\rm co}$ factor, the conversion factor of the ^{12}CO(J = 1–0) intensity to total molecular column density. The derived $X_{\rm co}$ factor was similar to that of other Local Group galaxies, such as the Small Magellanic Cloud, M31, M33, IC10, and the Milky Way, and the GMC mass distribution, dN/dM, was also similar to that of M31, M33, and IC10, suggesting that GMCs in the Local Group galaxies have similar properties (Fukui & Kawamura 2010; Blitz et al. 2007). Comparisons

between the GMCs and signs of star formation such as H II regions and young stellar clusters were used to classify GMCs into three types in terms of star formation activities (Fukui et al. 1999; Kawamura et al. 2009): Type I shows no signs of massive star formation, Type II is associated with only small H II regions, and Type III is associated with both H II regions and young stellar clusters, and these types are interpreted as an evolutionary sequence (Kawamura et al. 2009). Comparative studies of the ^{12}CO(J = 1–0)-to-H I ratio are also a key to understanding the evolution of GMCs and GMC formation via conversion of H I into H_2. Wong et al. (2009) made a two-dimensional, i.e., spatial, comparisons of the second NANTEN ^{12}CO(J = 1–0) survey (Fukui et al. 2008) with the H I data set combined with the ATCA and Parkes Telescope surveys (Kim et al. 2003). They found that significant H I column densities ($>10^{21}$ cm^{-2}) and peak brightness temperatures (>20 K) are necessary but insufficient conditions for CO detection. Fukui et al. (2009) compared the three-dimensional data cubes, including a velocity axis in addition to the two spatial axes. They found that GMCs are associated with H I envelopes on scales of ∼50–100 pc, and the H I envelopes may be in dynamical equilibrium or may be accreting onto GMCs to increase the mass via H I–H_2 conversion. Subsequently, a higher resolution (45″ ∼ 10 pc at 50 kpc) survey of the ^{12}CO(J = 1–0) molecular cloud with the Mopra 22 m telescope, the Magellanic Mopra Assessment (MAGMA), revealed a more detailed distribution of the ^{12}CO(J = 1–0) emission in the individual GMCs (Hughes et al. 2010). Hughes et al. (2010) demonstrated that the physical properties of star-forming GMCs are very similar to those of GMCs without signs of massive star formation.

Physical properties such as kinetic temperature and density of the molecular gas in the LMC have been investigated in the higher-J transitions (J = 2–1, J = 3–2, J = 4–3, J = 7–6) of CO (e.g., Sorai et al. 2001; Johansson et al. 1998; Heikkilä et al. 1999; Israel et al. 2003; Bolatto et al. 2005; Kim et al. 2004; Kim 2006; Nikolić et al. 2007; Pineda et al. 2008; Mizuno et al. 2010). Some authors (e.g., Bolatto et al. 2005; Nikolić et al. 2007) suggested a two-component model especially for molecular clouds closely associated with H II regions. Most of these studies targeted extraordinary H II regions so the sample is limited. Minamidani et al. (2008) carried out ^{12}CO(J = 3–2) observations of six GMCs, including one Type I, two Type II, and three Type III GMCs, in the LMC with the ASTE 10 m telescope at a spatial resolution of 5 pc, and identified 32 molecular clumps. These data were combined with available ^{12}CO(J = 1–0) and ^{13}CO(J = 1–0) data and compared with large velocity gradient (LVG) calculations for 13 clumps. The results show that these clumps range from cool (∼10–30 K) to warm (>30–200 K) in kinetic temperature, and warm clumps range from less dense (∼10^3 cm^{-3}) to dense (∼$10^{3.5}$–10^5 cm^{-3}), whereas only lower limits of kinetic temperature were obtained in the warm clumps. Most recently, Mizuno et al. (2010) have made ^{12}CO(J = 4–3) observations of the N159 region with the NANTEN2 4 m submillimeter telescope. These data were used in LVG analysis combined with ^{12}CO(J = 1–0), (J = 2–1), (J = 3–2), and (J = 7–6) as well as the isotope transitions of ^{13}CO(J = 1–0), (J = 2–1), (J = 3–2), and (J = 4–3). The kinetic temperatures and densities were found to be ∼70–80 K and ∼3 × 10^3 cm^{-3} in N159W and N159E, and ∼30 K and ∼1.6 × 10^3 cm^{-3} in N159S, indicating that an analysis including higher-J transitions of both ^{12}CO and ^{13}CO can better constrain kinetic temperature and density (Mizuno et al. 2010; Minamidani et al. 2009).

In the present study, we aim to determine the temperature and density of molecular hydrogen gas in all three GMC types, with higher accuracy by combining the ^{13}CO(J = 3–2) data newly obtained using the ASTE telescope and ^{12}CO(J = 3–2) and ^{13}CO(J = 1–0) data obtained with the ASTE and SEST telescopes, respectively. All our data sets are convolved to the same resolution of 45″, corresponding to ∼10 pc at a distance of the LMC, 50 kpc (Feast 1999), and LVG calculations are performed to estimate the line intensities.

Section 2 describes observations of the ^{13}CO(J = 3–2) transition. Section 3 gives the observational results and describes ancillary data sets. Section 4 contains the data analysis, and in Section 5, we discuss the physical properties of clumps and the evolutionary sequence of GMCs. In Section 6, we present the summary.

2. ^{13}CO(J = 3–2) OBSERVATIONS

2.1. Selection of Molecular Clumps

The present targets are chosen from the 32 molecular clumps identified by the ^{12}CO(J = 3–2) observations of the six GMCs in the LMC with the ASTE 10 m telescope at a spatial resolution of 5 pc (Minamidani et al. 2008). The six GMCs were chosen from the NANTEN catalog of ^{12}CO(J = 1–0) GMCs compiled by Fukui et al. (2008), and they comprised three Type III GMCs, two Type II GMCs, and one Type I GMC.

In the present study, we selected nine molecular clumps in the Type III GMCs, LMC N J0538−6904 (the 30 Doradus region; four clumps), and LMC N J0540−7008 (the N159 region; three clumps), Type II GMC, LMC N J0532−7114 (the N206D region; one clump), and Type I GMC, LMC N J0547−7041 (the GMC225 region; one clump). The observed clumps and their coordinates are listed in Table 1. Hereafter, the region names, which are in parentheses above or in Column 4 in Table 1, and the numbers of clumps, are used to identify the clumps, as in Minamidani et al. (2008). Among nine molecular clumps, four are in the 30 Doradus region, 30 Doradus No. 1, No. 2, No. 3, and No. 4, three are in the N159 region, N159 No. 1, No. 2, and No. 4, one is in the N206D region, N206D No. 1, and one is in the GMC225 region, GMC225 No. 1.

2.2. ^{13}CO(J = 3–2) Observations

The observations of the ^{13}CO(J = 3–2) transition at 330.587960 GHz were made with the ASTE 10 m telescope at Pampa la Bola in Chile in 2006 September. In this period, a single cartridge-type double-side-band (DSB) SIS receiver, SC345 (Kohno 2005), was installed and the XF-type digital autocorrelator (Sorai et al. 2000) was operated in the wideband mode, providing a bandwidth of 512 MHz with 1024 channels. These correspond to a velocity coverage of 450 km s^{-1} and a resolution of 0.45 km s^{-1} at 330 GHz. The half-power beam width was 23″ at 330 GHz, and this corresponds to 5.6 pc at 50 kpc. We made 3 × 3 points mapping observations with position switching method with a 20″ grid spacing toward the peaks of ^{12}CO(J = 3–2) clumps detected by Minamidani et al. (2008). Figure 1 shows the observed positions of the peaks of the ^{12}CO(J = 3–2) clumps named 30 Doradus No. 1, No. 2, No. 3, No. 4, N159 No. 1, No. 2, No. 4, N206D No. 1, and GMC225 No. 1. The typical system temperature including the atmosphere was 260 K in DSB. The pointing accuracy was measured to be better than 5″ peak to peak by periodically observing a CO point source R Dor in the ^{12}CO(J = 3–2) transition

Table 1
Observed Clumps and Properties of the ^{13}CO(J = 3–2) Line

GMC			Clump[a]				Peak Properties of ^{13}CO(J = 3–2) Line					Other ID[d]
No.[b]	Name[b]	Type[c]			Position		T_{mb}	V_{lsr}	ΔV	Integrated Intensity	rms	
			Region	No.	α(1950)	δ(1950)	(K)	(km s^{-1})	(km s^{-1})	(K km s^{-1})	(K)	
(1)	(2)	(3)	(4)	(5)	(6)	(7)	(8)	(9)	(10)	(11)	(12)	(13)
186	LMC N J0538−6904	III	30 Dor	1	5 39 08.6	−69 06 15	0.99	251.3	5.5	7.1	0.10	30Dor-10
				2	5 38 54.6	−69 08 00	0.86	247.4	5.2	5.2	0.09	30Dor-12
				3	5 38 49.0	−69 04 30	0.54	253.3	3.8	2.9	0.08	30Dor-06
				4	5 38 49.0	−69 03 30	0.47	249.0	3.8	2.2	0.08	
197	LMC N J0540−7008	III	N159	1	5 40 03.7	−69 47 00	3.2	237.9	5.8	23	0.18	N159W
				2	5 40 35.5	−69 46 00	1.7	233.1	3.7	8.4	0.11	N159E
				4	5 40 32.7	−69 52 00	0.60	237.0	3.5	3.2	0.07	N159S
156	LMC N J0532−7114	II	N206D	1	5 32 58.4	−71 15 20	1.6	225.4	3.0	5.7	0.09	
225	LMC N J0547−7041	I	GMC225	1	5 47 51.3	−70 41 20	0.19	216.9	2.2	0.33	0.04	

Notes. Units of R.A. are hours, minutes, and seconds and units of decl. are degrees, arcminutes, and arcseconds. Column 1: running number of GMC used in Table 1 in Fukui et al. (2008). Column 2: name of GMC. Column 3: type of GMC. Column 4: region name used in this paper. Column 5: running number of ^{12}CO(J = 3–2) clump in each region used in Table 2 in Minamidani et al. (2008). Columns 6 and 7: coordinates of the position of ^{12} the CO(J = 3–2) clump. Columns 8–12: observed properties of the ^{13}CO(J = 3–2) spectra obtained at the peak positions of the ^{12}CO(J = 3–2) clumps. The peak main-beam temperature T_{mb}, V_{LSR}, and the FWHM line width ΔV are derived from a single Gaussian curve fitting and are given in Columns 8, 9, and 10, respectively. The ^{13}CO(J = 3–2) integrated intensities and rms noise level at the peak positions of the ^{12}CO(J = 3–2) clumps are shown in Columns 11 and 12, respectively. Column 13: another identification based on ^{12}CO(J = 1–0) observations with SEST.

[a] Minamidani et al. (2008).
[b] Fukui et al. (2008).
[c] Kawamura et al. (2009).
[d] Johansson et al. (1998).

every 2 hr. The spectral intensities were calibrated by employing the standard room-temperature chopper-wheel method. We observed Ori-KL and M17SW in the ^{13}CO(J = 3–2) transition to check the stability of the intensity calibration, and the intensity variation during these observations was less than 12%.

The observed antenna temperature T_A^{OBS} varies with the sideband ratio or the image rejection ratio (IRR):

$$T_A^{OBS} = \frac{T_A^{SSB}}{1 + \frac{1}{IRR}},$$

where T_A^{SSB} is the antenna temperature in the single side band (SSB). We measured the antenna temperature, T_A^{OBS}, and IRR, simultaneously, with the newly installed 2SB receiver, CATS345 (Ezawa et al. 2008; Inoue et al. 2008), to the ASTE telescope in 2008, and derived the SSB antenna temperatures, T_A^{SSB}, of IRC+10216 [R.A.(1950) = 09^{h}45^{m}14^s.8, decl.(1950) = +13°30′40″] and N159W [R.A. (B1950) = 05^{h}40^{m}03^s.7, decl. (B1950) = −69°47′00.″0]. From the observation of IRC+10216, the velocity-integrated intensity, I.I.(T_A^{OBS}), was 56 ± 4 K km s^{-1} and the IRR was 6 ± 2 (∼8 dB). This IRR was consistent with the results of the laboratory evaluation (Inoue et al. 2008). The I.I.(T_A^{SSB}) was estimated to be 65 ± 6 K km s^{-1}. This value was compared with the data taken by CSO (Wang et al. 1994), and main-beam efficiency at that point was derived to be 0.70 ± 0.06. From the observation of N159W, the observed antenna temperature, T_A^{OBS}, was 1.83 ± 0.04 K, and the IRR was 4.7 ± 0.4 (∼7 dB). This IRR was consistent with the results of the laboratory evaluation (Inoue et al. 2008). The SSB antenna temperature, T_A^{SSB}, was estimated to be 2.22 ± 0.06 K. We derive the main-beam temperature, T_{mb} of N159W to be 3.2 ± 0.3 K. We scaled the observational data in 2006 to be consistent with this value. The achieved noise level ranged from 0.04 K to 0.18 K in the main-beam temperature scale. These observations were made remotely from NAOJ and NRO in Japan, using the network observation system N-COSMOS3 developed by NAOJ (Kamazaki et al. 2005).

3. RESULTS AND DATA SETS

3.1. ^{13}CO(J = 3–2)

In Figure 2, ^{13}CO(J = 3–2) profile maps of each observed peak are presented with ^{12}CO(J = 3–2) spectra (Minamidani et al. 2008). The ^{13}CO(J = 3–2) intensities are 3–12 times lower than those of ^{12}CO(J = 3–2). The peak velocities are consistent with those of ^{12}CO(J = 3–2), and the line widths are factor of 0.7–1.0 smaller than those of ^{12}CO(J = 3–2). Their line parameters at the peak positions of ^{12}CO(J = 3–2) are summarized in Table 1. Detailed descriptions explaining the characteristics of each observed ^{12}CO(J = 3–2) peak are given in the Appendix.

3.2. ^{12}CO(J = 3–2)

We use the ^{12}CO(J = 3–2) data published by Minamidani et al. (2008), which were taken by the ASTE telescope with an angular resolution of 22″. We measured the antenna temperature, T_A^{OBS}, and IRR, simultaneously, with the 2SB receiver, CATS345 (Ezawa et al. 2008; Inoue et al. 2008), newly installed on the ASTE telescope in 2008, and derived the SSB antenna temperatures, T_A^{SSB}, of IRC+10216 [R.A.(1950) = 09^{h}45^{m}14^s.8, decl.(1950) = +13°30′40″] and N159W [R.A. (B1950) = 05^{h}40^{m}03^s.7, decl. (B1950) = −69°47′00.″0]. From the observation of IRC+10216, the observed antenna temperature, T_A^{OBS}, was 18.8 ± 0.7 K, and the IRR was 22 ± 3 (∼13 dB). This IRR was consistent with the results of the laboratory evaluation (Inoue et al. 2008). The SSB antenna temperature, T_A^{SSB}, was estimated to be 19.6 ± 0.8 K. This value was compared with the data taken by CSO (Wang et al.

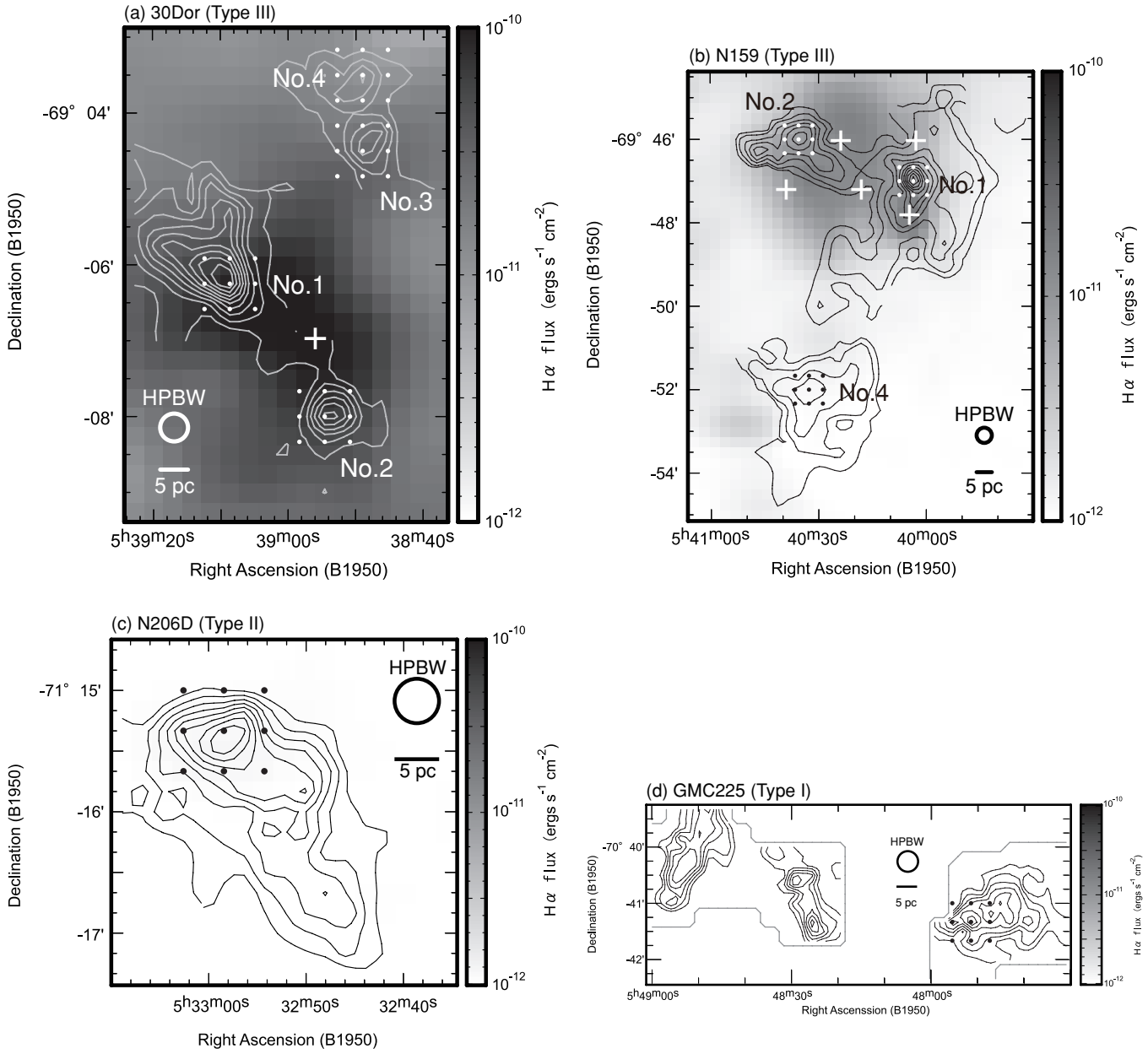

Figure 1. Positions observed with ^{13}CO(J = 3–2) in the (a) 30 Dor, (b) N159, (c) N206D, and (d) GMC225 regions. Observed positions are indicated with dots. Contours indicate integrated intensity of ^{12}CO(J = 3–2) and the gray scale indicates the Hα flux (Kim et al. 1999). White crosses indicate positions of young clusters (<10 Myr; SWB0).

1994), and main-beam efficiency at that point was derived to be 0.60 ± 0.02. From the observation of N159W, the observed antenna temperature, $T_{\rm A}^{\rm OBS}$, was 7.6 ± 0.2 K, and IRR was 9 ± 2 (∼10 dB). This IRR was consistent with the results of the laboratory evaluation (Inoue et al. 2008). The SSB antenna temperature, $T_{\rm A}^{\rm SSB}$, was estimated to be 8.4 ± 0.2 K. We derived the main-beam temperature, $T_{\rm mb}$ of N159W to be 13.9 ± 0.7 K. We scaled the observational data taken in 2004 (Minamidani et al. 2008) to be consistent with this value.

3.3. ^{13}CO(J = 1–0)

We use the ^{13}CO(J = 1–0) intensity of the 30 Doradus and N159 regions published by Johansson et al. (1998), and the N206D and GMC225 regions published by Minamidani et al. (2008). These data were all taken with the SEST telescope, and the angular resolution was 45″.

4. DATA ANALYSIS

4.1. Derivation of Line Intensity Ratios

The spatial resolutions of the present CO data vary depending on the telescope and frequency. The angular resolutions of ^{12}CO(J = 3–2) and ^{13}CO(J = 3–2) data observed by the ASTE telescope are 22″ and 23″, respectively, while that of ^{13}CO(J = 1–0) data observed by the SEST telescope are 45″. These correspond to ∼5 pc and 10 pc, respectively, at 50 kpc. We convolved the ^{12}CO(J = 3–2) and ^{13}CO(J = 3–2) data into the 45″ beam with a Gaussian smoothing function in order to derive physical properties of clumps whose sizes are around 10 pc.

We fitted Gaussian curves to each of the ^{12}CO(J = 3–2), ^{13}CO(J = 3–2), and ^{13}CO(J = 1–0) spectra with a single spectral peak. We derived the temperature peaks of the Gaussian

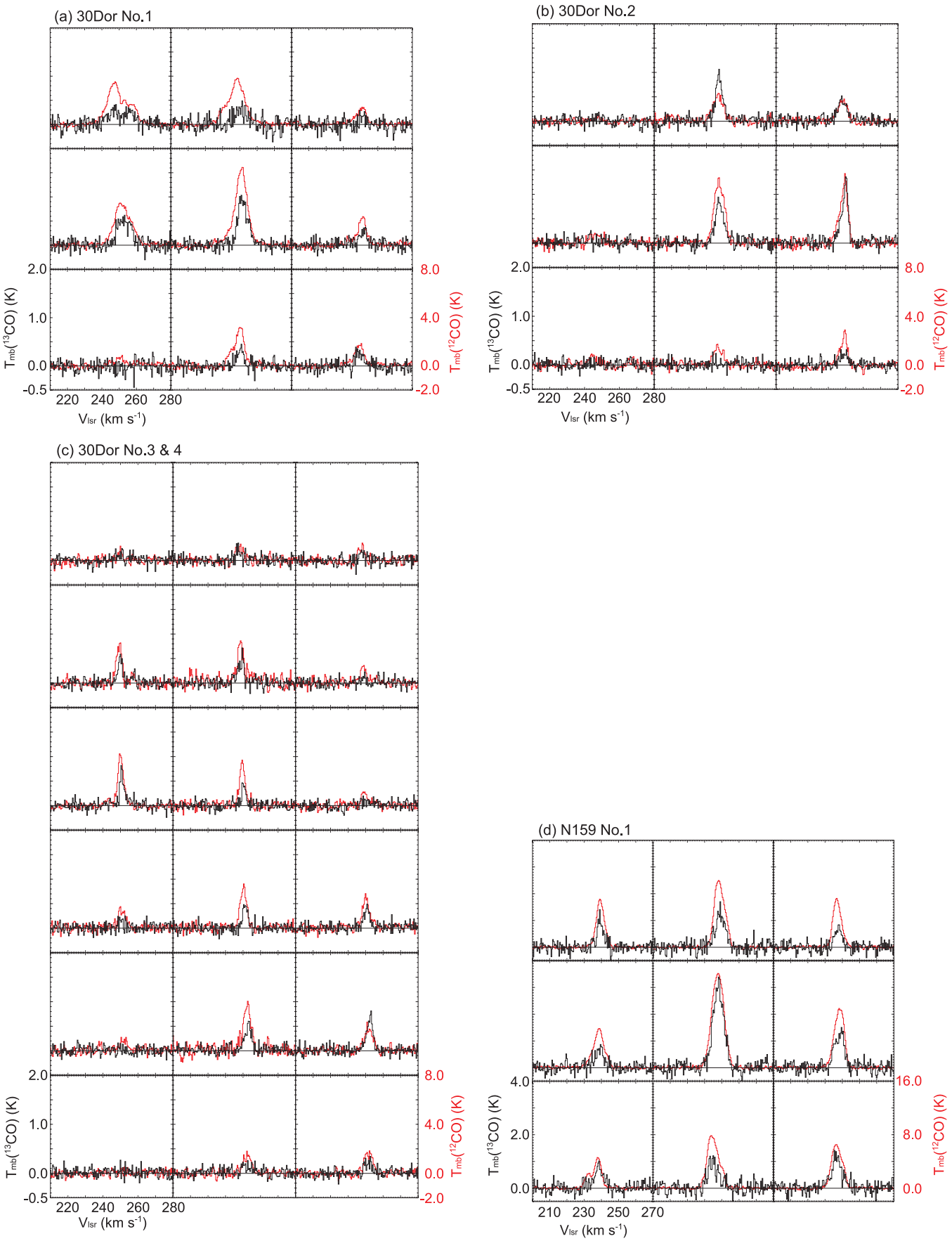

Figure 2. ^{13}CO(J = 3–2) profile maps of the (a) 30Dor No. 1, (b) 30Dor No. 2, (c) 30Dor Nos. 3 and 4, (d) N159 No. 1, (e) N159 No. 2, (f) N159 No. 4, (g) N206D No. 1, and (h) GMC225 No. 1 overlaid with ^{12}CO(J = 3–2) profiles. Black spectra are ^{13}CO(J = 3–2) and red ones are ^{12}CO(J = 3–2).

(A color version of this figure is available in the online journal.)

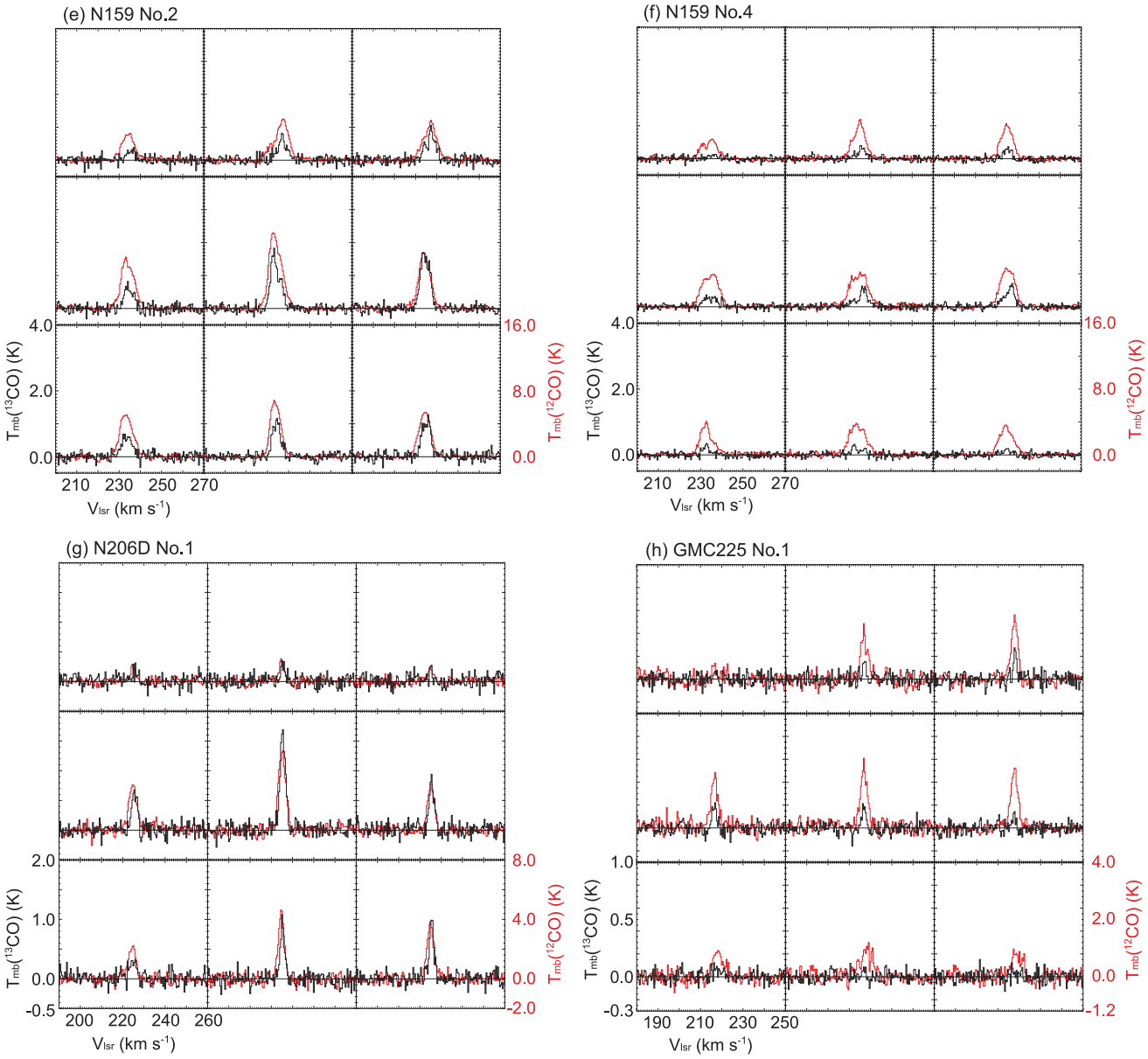

Figure 2. (Continued)

(A color version of this figure is available in the online journal.)

curves, and the results are summarized in Table 2. The ratios of ^{12}CO(J = 3–2) to ^{13}CO(J = 3–2) (hereafter, $R_{3-2}^{12/13}$) and ^{13}CO(J = 3–2) to ^{13}CO(J = 1–0) (hereafter, $R_{3-2/1-0}^{13}$) are derived as the ratios of the peak values on a main-beam temperature scale. The errors of $R_{3-2}^{12/13}$ and $R_{3-2/1-0}^{13}$ are estimated to be 20%–27% and 25%–30%, respectively. A summary of these main-beam temperature ratios and their accuracies are also presented in Table 2. These ratios will be compared with numerical calculations of radiative transfer in the LVG approximation to derive constraints on density and temperature.

4.2. LVG Analysis

4.2.1. Calculations of an LVG Model

In order to estimate the physical properties of the molecular gas, we have performed an LVG analysis (Goldreich & Kwan 1974) of the CO rotational transitions as described in Minamidani et al. (2008). The LVG radiative transfer code simulates a spherically symmetric cloud of uniform density and temperature with a spherically symmetric velocity gradient proportional to the radius, and employs a Castor's escape probability formalism (Castor 1970). It solves the equations of statistical equilibrium for the fractional population of CO rotational levels at each density and temperature, because the level populations of CO are determined by both the density and kinetic temperature of molecular hydrogen. It includes the lowest 40 rotational levels of the ground vibrational level and uses the Einstein A coefficient and H_2 collisional impact rate coefficients obtained from the Leiden Atomic and Molecular Database (Schöier et al. 2005).

We performed calculations of the fractional populations of the lowest 40 rotational levels of ^{12}CO and ^{13}CO in the ground vibrational state over a kinetic temperature range of $T_{\rm kin}$ = 5–200 K and a density range of $n(H_2)$ = 10–10^6 cm^{-3}.

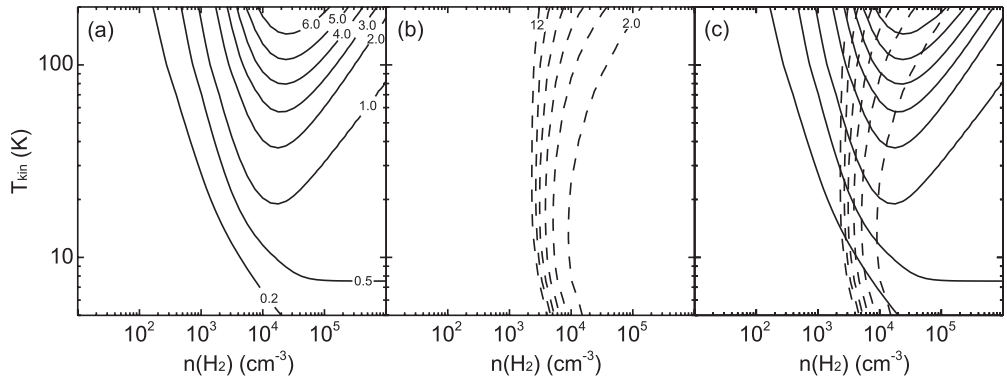

Figure 3. Contour plots of LVG analysis for reference. Contours are (a) $R^{13}_{3-2/1-0}$, (b) $R^{12/13}_{3-2}$, and (c) a + b. Here, $X(\mathrm{CO}) = 1.6 \times 10^{-5}$, $dv/dr = 1.0$ km s^{-1} pc^{-1}, and the number ratio (abundance ratio) ^{12}CO/^{13}CO is 50.

Table 2
Line Intensities and Line Ratios

Region	No.	Convolved $T_{\rm mb}$ (K)		$T_{\rm mb}$ (K)		Line Ratio		Hα flux
		^{13}CO(J = 3–2)	^{12}CO(J = 3–2)	^{13}CO(J = 1–0)	Ref.	$R^{12/13}_{3-2}$	$R^{13}_{3-2/1-0}$	($\times 10^{-12}$ erg s^{-1} cm^{-2})
(1)	(2)	(3)	(4)	(5)	(6)	(7)	(8)	(9)
30 Dor	1	0.47 ± 0.08	3.7 ± 0.5	0.13	J98	8.0 ± 1.7	3.6 ± 0.9	79
	2	0.46 ± 0.08	2.5 ± 0.4	···	J98	5.5 ± 1.2	···	59
	3	0.30 ± 0.06	2.0 ± 0.3	0.13	J98	6.7 ± 1.6	2.3 ± 0.6	21
	4	0.28 ± 0.06	2.3 ± 0.4	0.13	J98	8.2 ± 2.2	2.2 ± 0.6	10
N159	1	1.5 ± 0.2	8.6 ± 1.2	0.80	J98	5.7 ± 1.1	1.9 ± 0.5	6.0
	2	1.0 ± 0.1	6.1 ± 0.8	0.44	J98	6.1 ± 1.2	2.3±0.6	9.3
	4	0.36 ± 0.06	3.8 ± 0.5	0.72	J98	11 ± 2	0.50 ± 0.13	1.1
N206D	1	0.86 ± 0.12	3.3 ± 0.5	0.85	M08	3.8 ± 0.8	1.0 ± 0.2	1.2
GMC225	1	0.13 ± 0.03	1.5 ± 0.2	0.55	M08	12 ± 3	0.24 ± 0.07	0.94

Notes. Column 1: region. Column 2: running number in each region. Columns 3 and 4: the peak main-beam temperature, $T_{\rm mb}$, of ^{13}CO(J = 3–2) and ^{12}CO(J = 3–2), respectively, derived by using a single Gaussian curve fitting for a spectrum obtained by convolved spectra into the 45″ beam with a Gaussian kernel. Columns 5 and 6: the peak main-beam temperature, $T_{\rm mb}$, of ^{13}CO(J = 1–0) (Column 5) and their references (Column 6). Columns 7 and 8: ratios of the peak main-beam temperatures. Ratios of ^{12}CO(J = 3–2) to ^{13}CO(J = 3–2) are shown in Column 7 and that of ^{13}CO(J = 3–2) to ^{13}CO(J = 1–0) in Column 8. Column 9): Hα flux toward the peak positions.
References. (J98) Johansson et al. 1998; (M08) Minamidani et al. 2008.

We assumed that the fractional abundance of CO to H_2 and the abundance ratio of ^{12}CO to ^{13}CO are 1.6×10^{-5} and 50, respectively (Mizuno et al. 2010; Blake et al. 1987).

Figure 3 shows the general behavior of the loci of constant $R^{13}_{3-2/1-0}$ and constant $R^{12/13}_{3-2}$ in the density–temperature plane. The $R^{13}_{3-2/1-0}$ is the ratio of transitions which have different critical densities and traces the excitation of molecular gas. The $R^{12/13}_{3-2}$ is the ratio of transitions which have the same critical densities and traces different column densities, and thus this ratio is a good tracer of column density and consequently volume density in a wide temperature range. The combination of the two line ratios is nearly "orthogonal," so the density and kinetic temperature are well constrained. This is different from the case of Minamidani et al. (2008), who used the combination of the ratios of ^{12}CO(J = 3–2) to ^{12}CO(J = 1–0) (hereafter, $R^{12}_{3-2/1-0}$) and ^{12}CO(J = 1–0) to ^{13}CO(J = 1–0) (hereafter, $R^{12/13}_{1-0}$), which does not constrain well the physical parameters for densities higher than 10^4 cm^{-3} (Minamidani et al. 2008).

4.2.2. Results of the LVG Analysis

We summarize the input parameters for the eight clumps in Columns 3–5 of Table 3. The higher transition data have been convolved into the 45″ beam with a Gaussian kernel as described in Section 4.1. The velocity gradient, dv/dr, of each clump is derived from the ^{12}CO(J = 3–2) data (Minamidani et al. 2008).

Figure 4 shows the results of the LVG analysis for the eight clumps. The horizontal axis is the molecular hydrogen density, $n(H_2)$, and the vertical axis is the gas kinetic temperature, $T_{\rm kin}$. Solid lines represent $R^{13}_{3-2/1-0}$ and dashed lines represent $R^{12/13}_{3-2}$. The hatched areas indicate the overlap regions of these two ratios within the errors. In Table 3, we present the estimated densities and kinetic temperatures of the clumps.

The derived density and kinetic temperature are well determined compared to previous work based on the combination of $R^{12}_{3-2/1-0}$ and $R^{12/13}_{1-0}$ (Minamidani et al. 2008), especially for the clumps in the warm Type III GMCs. The results for the three clumps in the N159 region show good agreement with the results of Mizuno et al. (2010) who employed the calculations using high-J transitions of J = 4–3.

Figure 5 summarizes the derived kinetic temperatures ($T_{\rm kin}$) and densities ($n(H_2)$) of all eight clumps. These range from 15 to 200 K in kinetic temperature and from 8×10^2 to 7×10^3 cm^{-3} in density. We found that clumps in the 30 Doradus and N159 regions are warm and dense, except for N159 No. 4 (N159S), which is less dense and has an intermediate kinetic temperature. The clump in N206D, N206D No. 1, is dense and has an intermediate kinetic temperature. The clump in GMC225, GMC225 No. 1, is less dense and cold. The derived

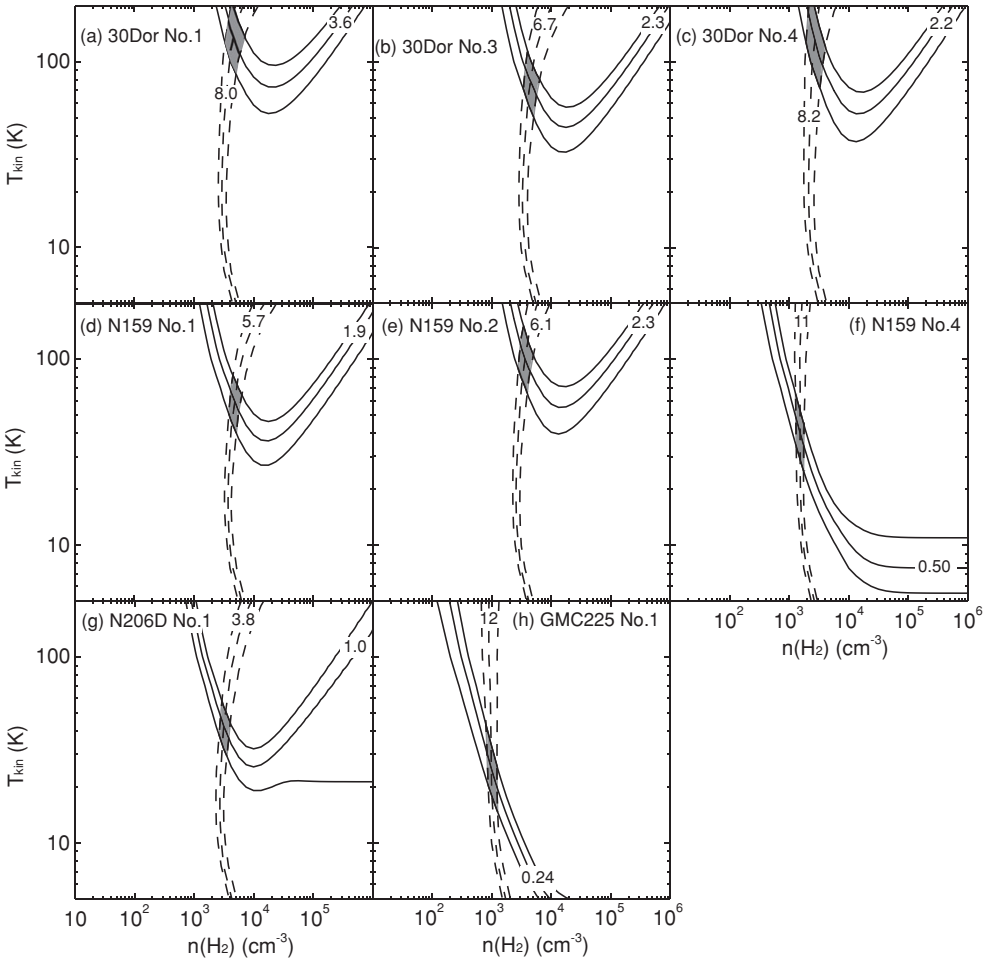

Figure 4. Contour plots of LVG analysis for eight clumps: (a) 30 Dor No. 1, (b) 30 Dor No. 3, (c) 30 Dor No. 4, (d) N159 No. 1, (e) N159 No. 2, (f) N159 No. 4, (g) N206D No. 1, and (h) GMC225 No. 1. The vertical axis is kinetic temperature $T_{\rm kin}$ and the horizontal axis is molecular hydrogen density $n(\rm H_2)$. Solid lines indicate $R^{13}_{3-2/1-0}$ and dashed lines indicate $R^{12/13}_{3-2}$. Hatched areas are the regions in which these two ratios overlap within intensity calibration errors.

Table 3
LVG Results

Region	No.	dv/dr (km s^{-1} pc^{-1})	$R^{12/13}_{3-2}$	$R^{13}_{3-2/1-0}$	$n(\rm H_2)$ ($\times 10^3$ cm^{-3})	$T_{\rm kin}$ (K)	Hα flux ($\times 10^{-12}$ erg s^{-1} cm^{-2})
(1)	(2)	(3)	(4)	(5)	(6)	(7)	(8)
30 Dor	1	0.9	8.0 ± 1.7	3.6 ± 0.9	$4.6^{+2.4}_{-1.3}$	134^{+66}_{-49}	79
	3	0.9	6.7 ± 1.6	2.3 ± 0.6	$4.5^{+1.9}_{-1.1}$	78^{+36}_{-27}	21
	4	0.5	8.2 ± 2.2	2.2 ± 0.6	$2.7^{+1.4}_{-0.8}$	131^{+69}_{-59}	10
N159	1	0.9	5.7 ± 1.1	1.9 ± 0.5	$4.9^{+1.5}_{-1.1}$	59^{+23}_{-19}	6.0
	2	0.5	6.1 ± 1.2	2.3 ± 0.6	$3.7^{+1.3}_{-0.9}$	100^{+51}_{-35}	9.3
	4	0.4	11 ± 2	0.50 ± 0.13	$1.5^{+0.3}_{-0.2}$	39^{+25}_{-14}	1.1
N206D	1	0.3	3.8 ± 0.8	1.0 ± 0.2	$3.2^{+0.9}_{-0.6}$	42^{+15}_{-13}	1.2
GMC225	1	0.2	12 ± 3	0.24 ± 0.07	$0.99^{+0.31}_{-0.19}$	25^{+18}_{-10}	0.94

Notes. Column 3: velocity gradient of clumps (Minamidani et al. 2008). Columns 6 and 7: results of LVG analysis.

kinetic temperature and density have the same tendency as indicated by Minamidani et al. (2008) with improved accuracy. For example, the kinetic temperature and density of the N159 No. 1 (N159W) clump are determined with accuracies of 39% and 31%, respectively, in the present work, although, in the previous study (Minamidani et al. 2008), only the lower limit of kinetic temperature (30 K) and two orders of magnitude uncertainty of density (3×10^3 to 8×10^5 cm^{-3}) were suggested for this clump.

4.2.3. Discussion of the LVG Results

There are two distinctive aspects of the present work. One is the continuous coverage of molecular clump samples in all three types of GMCs, which are interpreted as an evolutionary sequence (Kawamura et al. 2009). The other is the combinations of line ratios used in the LVG analysis. The ^{13}CO(J = 3–2), ^{12}CO(J = 3–2), and ^{13}CO(J = 1–0) transitions are used for the analysis and the ^{12}CO(J = 1–0) transition is not included

Table 4
Summary of an Excitation Analysis in the N159 Region

Paper	Reference	No. 1 (N159W)		No. 2 (N159E)		No. 4 (N159S)	
		T_{kin} (K)	$n(H_2)$ (10^3 cm^{-3})	T_{kin} (K)	$n(H_2)$ (10^3 cm^{-3})	T_{kin} (K)	$n(H_2)$ (10^3 cm^{-3})
(1)	(2)	(3)	(4)	(5)	(6)	(7)	(8)
This work	...	59^{+23}_{-19}	$4.9^{+1.5}_{-1.1}$	100^{+51}_{-35}	$3.7^{+1.3}_{-0.9}$	39^{+25}_{-14}	$1.5^{+0.3}_{-0.2}$
Mizuno10	M10	72^{+9}_{-9}	$4.0^{+0}_{-0.8}$	83^{+26}_{-20}	$3.1^{+1.9}_{-0.6}$	31^{+10}_{-8}	$1.6^{+0.4}_{-0.3}$
Pineda08	P08	80	10–100	...	...	...	...
Minamidani08	M08	> 30	3–800	> 40	1–300	20–60	1–6

References. (M10) Mizuno et al. 2010; (P08) Pineda et al. 2008; (M08) Minamidani et al. 2008.

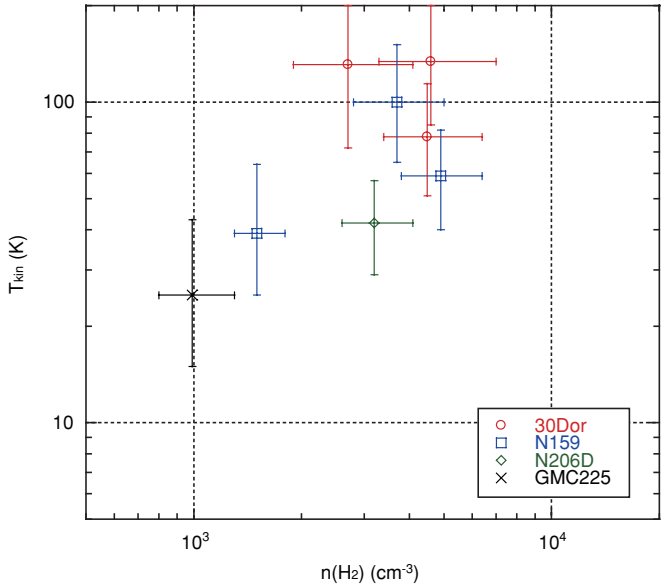

Figure 5. Plot of LVG results. The vertical axis is the kinetic temperature, T_{kin}, and the horizontal axis is the molecular hydrogen density, $n(H_2)$.
(A color version of this figure is available in the online journal.)

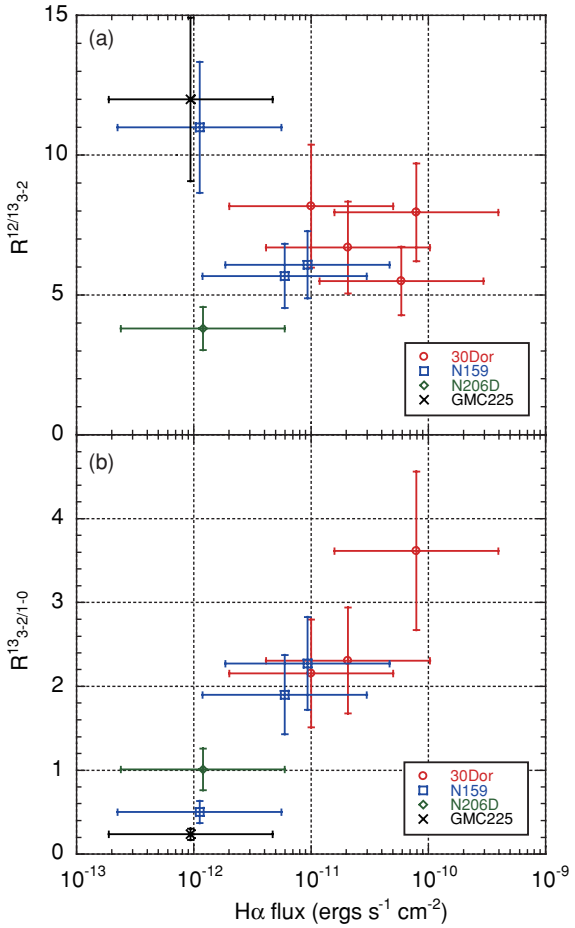

Figure 6. Relations between the line intensity ratio and the Hα flux. (a) Intensity ratio of ^{12}CO(J = 3–2) to ^{13}CO(J = 3–2), $R^{12/13}_{3-2}$. (b) Intensity ratio of ^{13}CO(J = 3–2) to ^{13}CO(J = 1–0), $R^{13}_{3-2/1-0}$.
(A color version of this figure is available in the online journal.)

in this work. This improves the accuracy of kinetic temperature and density of molecular clumps as described by Mizuno et al. (2010).

We also performed LVG calculations with the parameters used by Minamidani et al. (2008), which are $X(CO) = 3.0 \times 10^{-6}$ and abundance ratio of ^{12}CO to ^{13}CO of 20, 25, and 30. The kinetic temperatures and densities of clumps estimated from the $R^{12/13}_{3-2}$ and $R^{13}_{3-2/1-0}$ with these parameters were well determined. This indicates that the combinations of line intensity ratios used in this paper, $R^{12/13}_{3-2}$ and $R^{13}_{3-2/1-0}$, are suitable to determine physical properties of molecular clumps over wide ranges.

The N159 region is the most active site of high-mass star formation in the LMC. This has been observed in various molecular transitions by various telescopes located in the Southern Hemisphere, and many authors have attempted to determine the physical properties and chemical compositions via LVG analyses (e.g., Mizuno et al. 2010; Pineda et al. 2008; Minamidani et al. 2008). In Table 4, some of the recent LVG results of the N159 region are summarized. The kinetic temperature and density derived in this work are consistent within errors with those derived by Mizuno et al. (2010) and Pineda et al. (2008), which are determined with high accuracy based on data of higher transitions of J = 4–3 and J = 7–6.

4.3. Comparison of Line Intensity Ratios and Physical Properties with Hα Flux

We use the Hα data (Kim et al. 1999) toward the present clouds using the method given in Appendix B of Minamidani et al. (2008). The typical background level of Hα flux is $\sim 10^{-12}$ erg s^{-1} cm^{-2} at the 40″ scale, which is a pixel scale of the Hα data. These data were regridded into the ^{13}CO(J = 3–2) data grids. The fluxes toward each ^{13}CO(J = 3–2) peak are listed in Tables 2 and 3.

Figure 6 shows plots of $R^{12/13}_{3-2}$ and $R^{13}_{3-2/1-0}$ as functions of Hα flux. It is clear that $R^{13}_{3-2/1-0}$ is well correlated with the Hα

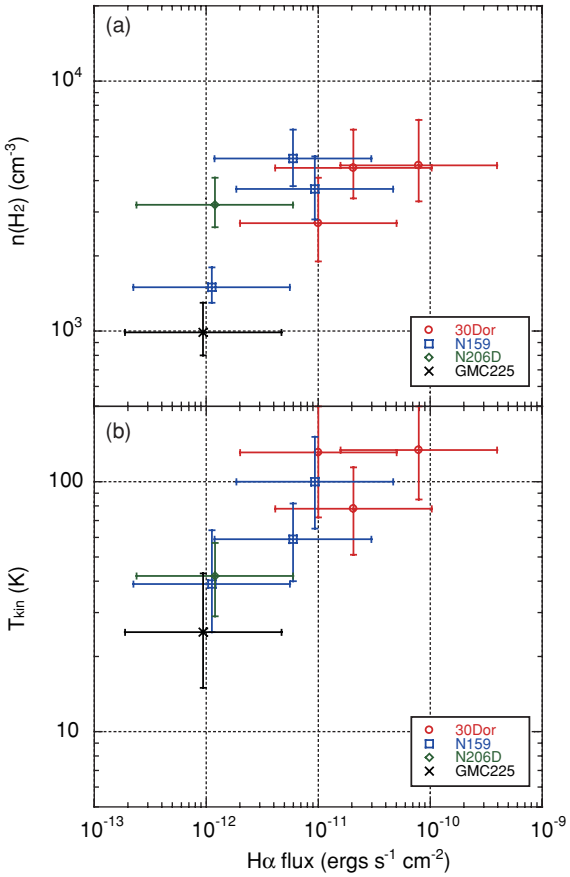

Figure 7. Plot of physical properties as a function of Hα flux at the ^{12}CO(J = 3–2) peak. The vertical axes are (a) the molecular hydrogen density, $n(H_2)$, and (b) the kinetic temperature, T_{kin}. The horizontal axis is the Hα flux.

(A color version of this figure is available in the online journal.)

flux with a correlation coefficient of 0.98, and there is no clear correlation between $R^{12/13}_{3-2}$ and Hα flux.

Figure 7 shows plots of molecular hydrogen densities, $n(H_2)$, and kinetic temperatures, T_{kin}, as functions of Hα flux. For dense clumps these are distributed over a wide range of Hα flux (10^{-12}–10^{-10} erg s^{-1} cm^{-2}), although lower density clumps are located only where the Hα flux is weak ($\sim 10^{-12}$ erg s^{-1} cm^{-2}). The T_{kin} of the clumps is well correlated with the Hα flux with a correlation coefficient of 0.81. We note that the size scale here is 10 pc and the good correlation may not hold at smaller scales where local extinction of Hα becomes important (e.g., Mizuno et al. 2010). These results suggest that FUV photons heat molecular gas whose density is 10^3–10^4 cm^{-3}. This will be discussed in the following section.

5. DISCUSSION

5.1. Evolutions of GMC and Clump

The results of our LVG analysis show that the clump kinetic temperatures, T_{kin}, range from cool ($\sim$15 K) to warm ($\sim$200 K) and the densities, $n(H_2)$, from less dense ($\sim 8 \times 10^2$ cm^{-3}) to dense ($\sim 7 \times 10^3$ cm^{-3}). These large variations in the physical properties reflect the different characteristics of the GMCs according to their Types I, II, and III, where Type I shows no signs of massive star formation, Type II is associated with only small H II regions, and Type III is associated with both H II regions and young stellar clusters, and these types are interpreted as an evolutionary sequence (Kawamura et al. 2009).

A clump in a Type I GMC, GMC225 No. 1, has the lowest density ($n(H_2) \sim 0.99 \times 10^2$ cm^{-3}) and lowest temperature ($T_{kin} \sim 25$ K). A clump in Type II GMC, N206D No. 1, is dense ($n(H_2) \sim 3.2 \times 10^3$ cm^{-3}) and has intermediate temperature ($T_{kin} \sim 42$ K). Clumps in Type III GMCs, except for N159 No. 4 (N159S), are dense ($n(H_2) \sim 4 \times 10^3$ cm^{-3}) and warm ($T_{kin} >$ 50 K). The physical properties are generally correlated with the star formation activity of GMCs. T_{kin} and $n(H_2)$ increase with the evolution of GMCs from Type I to III. This trend becomes clearer with the present determination of T_{kin} and $n(H_2)$ than that of the previous study (Minamidani et al. 2008), although the samples are smaller.

The N159 No. 4 (N159S) clump is a part of a Type III GMC, LMC N J0540−7008 (Kawamura et al. 2009). This GMC is quite large and elongated from north to south (275 pc × 53 pc, P.A. = 87°; Fukui et al. 2008). Young clusters and large H II regions are associated with the northern part of this GMC, but not with the southern part, where N159 No. 4 (N159S) is located. The N159 No. 4 (N159S) clump is less dense ($n(H_2) \sim 1.5 \times 10^3$ cm^{-3}) and has intermediate temperature ($T_{kin} \sim 39$ K). These properties are similar to those of the clumps in Type I or II GMCs, as discussed by Minamidani et al. (2008) and Mizuno et al. (2010). Comparison of the properties of molecular clumps with signs of star formation activity, such as young star clusters and Hα emission at high spatial resolution, will establish the classification of molecular clumps, whose sizes are $\sim$7 pc (Minamidani et al. 2008). Because the sizes of clusters in the LMC are distributed in a range from 0.1–10 pc (Hunter et al. 2003), which is smaller than/similar to the typical size of molecular clumps ($\sim$7 pc), it is important to compare molecular clumps with signs of star/cluster formation to understand the corresponding evolution.

5.2. Heating of the Molecular Gas in the LMC

As discussed in the previous sections, the $R^{13}_{3-2/1-0}$ is well correlated with the Hα flux at a 10 pc scale, and so are the molecular gas kinetic temperatures (T_{kin}). These findings suggest that the heating of molecular gas whose density is 10^3–10^4 cm^{-3} may be dominated by FUV photons. The intense FUV field controls the physical and chemical processes in the ISM such as formation and destruction of molecules as well as ionization. These regions have been modeled as photo-dissociation regions or photon-dominated regions (PDRs) (e.g., Tielens & Hollenbach 1985; Kaufman et al. 1999; Röllig et al. 2007 and references therein).

The FUV flux (G_0) is estimated to be 3500 in the 30 Doradus region (Bolatto et al. 1999; Poglitsch et al. 1995; Werner et al. 1978; Israel & Koornneef 1979) and 300 for the N159 region (Bolatto et al. 1999; Israel et al. 1996; Israel & Koornneef 1979). The gas density is estimated to be (1–5)×10^3 cm^{-3} for these regions. The PDR surface temperature is $\sim$400 K for the 30 Doradus region and $\sim$200 K for the N159 region from Figure 1 of Kaufman et al. (1999). The PDR gas temperature is relatively constant from the cloud surface to a depth where either heating or cooling changes significantly. The heating is generally dominated by the grain photoelectric heating (Kaufman et al. 1999), and then dust attenuation of FUV flux controls the thermal structure, where the typical size is 0.1–2 pc. These suggest that the effect of FUV heating of molecular gas seems to be local and direct phenomena.

The warm region can become larger under low-metallicity or high gas-to-dust ratio environments. These temperatures are basically consistent with the kinetic temperatures (T_{kin}) of the

warm clumps in the present sample if beam dilution by the present resolution, 10 pc, is taken into account.

5.3. Substructures Inferred by the $^{13}CO(J = 3–2)$ Observations

The $^{13}CO(J = 3–2)$ intensities are 3–12 times lower than those of $^{12}CO(J = 3–2)$ transition, and the line intensity ratios of $^{12}CO(J = 3–2)$ to $^{13}CO(J = 3–2)$, $R_{3-2}^{12/13}$, vary not only from clump to clump but also inside each clump. In some clumps, two clear velocity components are detected in the $^{13}CO(J = 3–2)$ transition. These suggest some internal structure.

Mizuno et al. (2010) showed that the molecular distribution of the N159 No. 1 (N159W) clump in the $^{12}CO(J = 3–2)$ transition is similar to that of the η Carinae northern cloud in the $^{12}CO(J = 1–0)$ emission line smoothed to a 5 pc resolution. The original data of the η Carinae northern cloud have a 2 pc resolution and several substructures are identified (Yonekura et al. 2005). This supports the existence of internal structures inside ~5 pc scale molecular clumps and indicates that these internal structures can be resolved in the CO transitions with high spatial resolution observations.

Subsequent observations of the η Carinae northern cloud using a high-density tracer such as $H^{13}CO^+(J = 1–0)$ at a high spatial resolution resulted in the detection of high-density molecular cores whose sizes are less than 1 pc (Yonekura et al. 2005). In the LMC, some initial interferometric observations of high-density tracers, such as HCO^+ and NH_3, were made with ATCA, using resolutions of ~6″–19″ corresponding to ~1.4–5 pc at 50 kpc (e.g., Wong et al. 2006; Ott et al. 2008, 2010). Ott et al. (2008) detected two peaks in the $HCO^+(J = 1–0)$ transition in the N159W region. Further systematic detailed observations using high-density tracers at higher resolution, with ALMA, for instance, should be important for probing the initial conditions for star/cluster formation.

6. SUMMARY

We have made 3 × 3 point mapping observations in the $^{13}CO(J = 3–2)$ transition at 330 GHz using the ASTE 10 m telescope toward nine peaks of $^{12}CO(J = 3–2)$ clumps, which cover all types of GMCs, Type I, II, and III, which are interpreted as an evolutionary sequence of GMCs. We have detected the $^{13}CO(J = 3–2)$ emission from all peaks and their intensities are 3–12 times lower than those of $^{12}CO(J = 3–2)$. From this, we have derived the intensity ratios of $^{12}CO(J = 3–2)$ to $^{13}CO(J = 3–2)$, $R_{3-2}^{12/13}$, and $^{13}CO(J = 3–2)$ to $^{13}CO(J = 1–0)$, $R_{3-2/1-0}^{13}$, at 45″ resolution, and compared these results with the LVG radiative transfer calculations in order to estimate kinetic temperatures, T_{kin}, and densities, $n(H_2)$, of the eight clumps. The clumps show T_{kin} = 15–200 K and $n(H_2)$ = 8×10^2–7×10^3 cm^{-3}. The Hα flux toward these clumps is well correlated with the $^{13}CO(J = 3–2)/^{13}CO(J = 1–0)$ ratio, $R_{3-2/1-0}^{13}$, and with the kinetic temperatures, T_{kin}, of the clumps. Dense clumps are distributed over a wide range of Hα flux (10^{-12}–10^{-10} erg s^{-1} cm^{-2}), although lower density clumps are located only where the Hα flux is weak (~10^{-12} erg s^{-1} cm^{-2}). We found that clumps in the 30 Doradus and N159 regions (Type III GMCs) are warm and dense, except for N159 No. 4 (N159S), which is less dense and has intermediate kinetic temperature. The clump in N206D (Type II GMC), N206D No. 1, is dense and also has intermediate kinetic temperature. The clump in GMC225 (Type I GMC), GMC225 No. 1, is less dense and cold. We suggest that differences of these clump properties largely reflect an evolutionary sequence of GMCs and molecular clumps. The kinetic temperatures (T_{kin}) and densities ($n(H_2)$) of molecular clumps increase generally with the evolution of GMCs and molecular clumps. The $R_{3-2/1-0}^{13}$ and kinetic temperatures (T_{kin}) are well correlated with the Hα flux, suggesting that the heating of molecular gas whose density ($n(H_2)$) = 10^3–10^4 cm^{-3} is dominated by FUV photons. The calculations of the PDR models are consistent with this suggestion.

A part of this study was financially supported by MEXT Grant-in-Aid for Specially Promoted Research (20001003). T.M. was supported by JSPS Research Fellowships for Young Scientists. M.R. wishes to acknowledge support from FONDECYT(CHILE) grant No. 1080335 and the Chilean Center for Astrophysics FONDAP No. 15010003. S.K. was supported in part by the National Research Foundation of Korea (NRF) grant funded by the Korean government (MEST) 2010-0017231.

The ASTE project is managed by Nobeyama Radio Observatory (NRO), a branch of the National Astronomical Observatory of Japan (NAOJ), in collaboration with University of Chile, and Japanese institutes including University of Tokyo, Nagoya University, Osaka Prefecture University, Ibaraki University, and Hokkaido University. Observations with ASTE were carried out remotely from Japan by using NTT's GEMnet2 and its partner R&E (Research & Education) networks, which are based on the AccessNova collaboration of University of Chile, NTT Laboratories, and NAOJ.

Facilities: ASTE (SC345-MAC), SEST

APPENDIX

DETAILED DESCRIPTIONS OF EACH CLUMP

30 Doradus No. 1 (30Dor-10) (Figure 2(a)). The measured noise level of $^{13}CO(J = 3–2)$ spectra in this region is 0.10 K rms at 0.45 km s^{-1} velocity resolution. The spatial extent and velocity range of the $^{13}CO(J = 3–2)$ emission are well correlated to those of the $^{12}CO(J = 3–2)$ emission. The ratios of integrated intensities of $^{12}CO(J = 3–2)$ to $^{13}CO(J = 3–2)$ (hereafter $R_{3-2,II}^{12/13}$) are relatively small (~6) at the western position and relatively large (~19) at the northern position.

30 Doradus No. 2 (30Dor-12) (Figure 2(b)). The measured noise level of $^{13}CO(J = 3–2)$ spectra in this region is 0.09 K rms at 0.45 km s^{-1} velocity resolution. The spatial extent and the velocity range of the $^{13}CO(J = 3–2)$ emission are well correlated to those of the $^{12}CO(J = 3–2)$ emission. $R_{3-2,II}^{12/13}$ at the northern position is ~3, the smallest value among this clump, and is larger than 15 at the southern position.

30 Doradus Nos. 3 and 4 (30Dor-06) (Figure 2(c)). The southern part corresponds to No. 3 clump and the northern part corresponds to No. 4 clump. The measured noise level of $^{13}CO(J = 3–2)$ spectra in this region is 0.08 K rms at 0.45 km s^{-1} velocity resolution. The spatial extent and the velocity range of the $^{13}CO(J = 3–2)$ emission are well correlated to those of the $^{12}CO(J = 3–2)$ emission.

N159 No. 1 (N159W) (Figure 2(d)). The measured noise level in this region is 0.18 K rms at 0.45 km s^{-1} velocity resolution. The spatial extent and the velocity range of the $^{13}CO(J = 3–2)$ emission are well correlated to those of the $^{12}CO(J = 3–2)$ emission. $R_{3-2,II}^{12/13}$ shows the smallest value of ~5

in this clump at the central position. At the southwest position, the $R^{12/13}_{3-2,\mathrm{II}}$ is also small (∼6). At the northwest position, the ratio is large of ∼15.

N159 No. 2 (N159E) (Figure 2(e)). The measured noise level in this region is 0.11 K rms at 0.45 km s^{-1} velocity resolution. The spatial extent and velocity range of the ^{13}CO(J = 3–2) emission are well correlated to those of the ^{12}CO(J = 3–2) emission. $R^{12/13}_{3-2,\mathrm{II}}$ shows the smallest value of ∼5 in this clump at the western position and a large value of ∼15 at the northeast position.

N159 No. 4 (N159S) (Figure 2(f)). The measured noise level in this region is 0.07 K rms at 0.45 km s^{-1} velocity resolution. The spatial extent and the velocity range of the ^{13}CO(J = 3–2) emission are well correlated to those of the ^{12}CO(J = 3–2) emission. Intensities of the ^{13}CO(J = 3–2) emission are fairly weak compared to those of the ^{12}CO(J = 3–2) emission. $R^{12/13}_{3-2,\mathrm{II}}$ shows the smallest value of ∼12 in this clump at the center position. Two velocity components are detected in the ^{13}CO(J = 3–2) transition, although only one component is detected in the ^{12}CO(J = 3–2) transition.

N206D No. 1 (Figure 2(g)). The measured noise level in this region is 0.09 K rms at 0.45 km s^{-1} velocity resolution. The spatial extent and the velocity range of the ^{13}CO(J = 3–2) emission are well correlated to those of the ^{12}CO(J = 3–2) emission.

GMC225 No. 1 (Figure 2(h)). The measured noise level in this region is 0.04 K rms at 0.45 km s^{-1} velocity resolution. The spatial extent and velocity range of the ^{13}CO(J = 3–2) emission are well correlated to those of the ^{12}CO(J = 3–2) emission. Intensities of the ^{13}CO(J = 3–2) emission are ∼12 times weaker than those of the ^{12}CO(J = 3–2) emission.

REFERENCES

Blake, G. A., Sutton, E. C., Masson, C. R., & Phillips, T. G. 1987, ApJ, 315, 621
Blitz, L., Fukui, Y., Kawamura, A., Leroy, A., Mizuno, N., & Rosolowsky, E. 2007, in Protostarts and Planets V, ed. B. Reipurth, D. Jewitt, & K. Keil (Tucson, AZ: Univ. Arizona Press), 81
Bolatto, A. D., Israel, F. P., & Martin, C. L. 2005, ApJ, 633, 210
Bolatto, A. D., Jackson, J. M., & Ingalls, J. G. 1999, ApJ, 513, 275
Castor, J. I. 1970, MNRAS, 149, 111
Dufour, R. J. 1984, in IAU Symp. 108, Structure and Evolution of the Magellanic Clouds, ed. S. van den Bergh & K. S. de Boer (Dordrecht: Reidel), 353
Ezawa, H., et al. 2008, Proc. SPIE, 7012, 701208
Feast, M. 1999, in IAU Symp. 190, New Views of the Magellanic Clouds, ed. Y.-H. Chu, et al. (Cambridge: Cambridge Univ. Press), 542
Fukui, Y., & Kawamura, A. 2010, ARA&A, 48, 547
Fukui, Y., et al. 1999, PASJ, 51, 745
Fukui, Y., et al. 2001, PASJ, 53, L41
Fukui, Y., et al. 2008, ApJS, 178, 56
Fukui, Y., et al. 2009, ApJ, 705, 144
Goldreich, P., & Kwan, J. 1974, ApJ, 189, 441
Heikkilä, A., Johansson, L. E. B., & Olofsson, H. 1999, A&A, 344, 817
Hodge, P. W. 1961, ApJ, 133, 413
Hughes, A., et al. 2010, MNRAS, 406, 2065
Hunter, D. A., Elmegreen, B. G., Dupuy, T. J., & Mortonson, M. 2003, AJ, 126, 1836
Inoue, H., Muraoka, K., Sakai, T., Endo, A., Kohno, K., Asayama, S., Noguchi, T., & Ogawa, H. 2008, in Proc. 19th Int. Symp. Space THz Technolgy, ed. W. Wild, 281
Israel, F. P., de Graauw, Th., van de Stadt, H., & de Vries, C. P. 1986, ApJ, 303, 186
Israel, F. P., & Koornneef, J. 1979, ApJ, 230, 390
Israel, F. P., Maloney, P. R., Geis, N., Herrmann, F., Madden, S. C., Poglitsch, A., & Stacey, G. J. 1996, ApJ, 465, 738
Israel, F. P., et al. 2003, A&A, 401, 99
Johansson, L. E. B., et al. 1998, A&A, 331, 857
Kamazaki, T., et al. 2005, in ASP Conf. Ser. 347, Astronomical Data Analysis Software and Systems, ed. P. Shopbell, M. Britton, & R. Ebert (San Francisco, CA: ASP), 533
Kaufman, M. J., Wolfire, M. G., Hollenbach, D. J., & Luhman, M. L. 1999, ApJ, 527, 795
Kawamura, A., et al. 2009, ApJS, 184, 1
Keller, S. C., & Wood, P. R. 2006, ApJ, 642, 834
Kim, S. 2006, PASP, 118, 94
Kim, S., Dopita, M. A., Stavely-Smith, L., & Bessell, M. S. 1999, AJ, 118, 2797
Kim, S., Staveley-Smith, L., Dopita, M. A., Sault, R. J., Freeman, K. C., Lee, Y., & Chu, Y.-H. 2003, ApJS, 148, 473
Kim, S., Walsh, W., & Xiao, K. 2004, ApJ, 616, 865
Kohno, K. 2005, in ASP Conf. Ser. 344, The Cool Universe: Observing Cosmic Dawn, ed. C. Lidman & D. Alloin (San Francisco, CA: ASP), 242
Koornneef, J. 1984, in IAU Symp. 108, Structure and Evolution of the Magellanic Clouds, ed. S. van den Bergh & K. S. de Boer (Dordrecht: Reidel), 333
Minamidani, T., et al. 2008, ApJS, 175, 485
Minamidani, T., et al. 2009, in IAU Symp. 256, The Magellanic Clouds: Stars, Gas, and Galaxies, ed. J. Th. van Loon & J. M. Oliveira (Cambridge: Cambridge Univ. Press), 256
Mizuno, N., et al. 2001, PASJ, 53, 971
Mizuno, Y., et al. 2010, PASJ, 62, 51
Nikolić, S., et al. 2007, A&A, 471, 561
Ott, J., et al. 2008, PASA, 25, 129
Ott, J., et al. 2010, ApJ, 710, 105
Pineda, J. L., et al. 2008, A&A, 482, 197
Poglitsch, A., Krabbe, A., Madden, S. C., Nikola, T., Geis, N., Johansson, L. E. B., Stacey, G. J., & Sternberg, A. 1995, ApJ, 454, 293
Rolleston, W. R. J., Trundle, C., & Dufton, P. L. 2002, A&A, 396, 53
Röllig, M., et al. 2007, A&A, 467, 187
Schöier, F. L., van der Tak, F. F. S., van Dichoeck, E. F., & Black, J. H. 2005, A&A, 432, 369
Sorai, K., et al. 2000, Proc. SPIE, 4015, 86
Sorai, K., et al. 2001, ApJ, 551, 794
Tielens, A. G. G. M., & Hollenbach, D. 1985, ApJ, 291, 722
van der Marel, R., & Cioni, M.-R. L. 2001, AJ, 122, 1807
Wang, Y., Jaffe, D. T., Graf, U. U., & Evans, N. J., II 1994, ApJS, 95, 503
Werner, M. W., Becklin, E. E., Gatley, I., Ellis, M. J., Hyland, A. R., Robinson, G., & Thomas, J. A. 1978, MNRAS, 184, 365
Wong, T., Whiteoak, J. B., Ott, J., Chin, Y., & Cunningham, M. R. 2006, ApJ, 649, 224
Wong, T., et al. 2009, ApJ, 696, 370
Yonekura, Y., Asayama, S., Kimura, K., Ogawa, H., Kanai, Y., Yamaguchi, N., Barnes, P. J., & Fukui, Y. 2005, ApJ, 634, 476